Nanoparticle-Assembled Capsule Synthesis: Formation of Colloidal Polyamine−Salt Intermediates

Vinit S. Murthy,[†] Rohit K. Rana,[†,§] and Michael S. Wong*,[†,‡]

Department of Chemical and Biomolecular Engineering, Rice University, Houston, Texas 77251-1892, and Department of Chemistry, Rice University, Houston, Texas 77251-1892

Received: March 23, 2006; In Final Form: September 11, 2006

There is current interest in developing new synthesis strategies for multifunctional hollow spheres with tunable structural properties that would be useful in encapsulation and controlled release applications. A new route was reported recently, in which the sequential reaction of polyamines, multivalent anions, and charged nanoparticles leads to the formation of polymer-filled and water-filled organic/inorganic micron-sized structures known as nanoparticle-assembled capsules. This technique is unique among other capsule preparation routes, as it allows the rapid and scalable formation of robust shells at room temperature, in near-neutral water, and with readily available precursors. This nanoparticle assembly synthesis route involves two steps: the formation of polymer aggregates and the subsequent deposition of particles around the aggregates. The purpose of this paper is to understand in greater detail the noncovalent chemistry of the polymer−salt aggregation step. With poly(allylamine hydrochloride) (PAH) as the model polymer, aggregate formation was investigated as a function of charge ratio, pH, and time through dynamic light scattering, electrophoretic mobility measurements, chloride ion measurements, and optical microscopy. PAH formed aggregates by the cross-linking action of divalent and higher-valent anions above a critical charge ratio and in a pH range defined by the pK_a values of PAH and the anion. The aggregates grew in size through coalescence and with growth rates that depended on their surface charge. Controlling polymer aggregate growth provided a direct and simple means to adjust the size of the resultant capsule materials.

Introduction

The hollow sphere (or, alternatively, the closed-shell or capsule structure) is a basic structural motif in materials design in which a discrete volume is compartmentalized and isolated from the exterior by a closed-shell barrier. Depending on their application, hollow spheres can be filled or empty. They function as encapsulation, protection, and delivery agents and are used in application areas as diverse as medicine, foods, cosmetics, and paints.[1−8] As part of a matrix composite, hollow spheres are being developed as low dielectric constant materials and acoustic insulation.[9]

Efforts in hollow sphere synthesis in the last 15 years have aimed toward smaller sizes, in the micron (>1000 nm), submicron (100−1000 nm), and nanometer (1−100) range, narrower size distributions, greater functionality, and scalable production. The preparation methods can be broadly categorized into self-assembly, sacrificial core templating, and physical formation. Self-assembly routes encompass the thermodynamically driven arrangements of amphiphilic organic compounds, in which contact between the hydrocarbon tail groups and water is minimized. Examples of such systems include lipid vesicles,[1] diblock copolymer vesicles,[10−12] virus particles,[13] and supramolecular cage structures.[14] Their preparation and their encapsulation of soluble compounds can be readily carried out, but the structures are sensitive to the water environment and disintegrate

upon the removal of water. The sacrificial core templating approach can yield stable hollow spheres with uniform diameters if solid particles are used as the template and a thick shell is formed. The shell is formed around the solid template through sol−gel chemistry,[8,15−17] polymerization,[18] adsorption of smaller particles,[19,20] and multilayer adsorption of colloidal species via layer-by-layer assembly.[8,21−24] The core is then removed via chemical dissolution or high-temperature combustion to produce free-standing, hollow spheres. Besides latex particles, other materials can be used as the template, such as metal nanoparticles, vesicles, micelles, emulsion droplets, and inverse opals.[16,19,25−29] This approach is highly flexible, although it requires more processing steps than the self-assembly routes. Encapsulation of desired compounds is not trivial, however, as the template removal step must be carried out in such a way as to not damage the encapsulated compounds. Through physical formation methods, micron-sized and even submicron-sized hollow spheres can be generated in a continuous manner, using specialized spray-drying and electrified coaxial jetting equipment to form liquid droplets as the templating core.[30−32]

We recently reported a new approach to preparing stable hollow microspheres through a simple two-step mixing procedure involving negatively charged nanoparticles (NPs), cationic polymer, and multivalent anions.[33] Termed "tandem self-assembly" or "polymer aggregate templating," this process involves combining the polymer and salt to form polymer−salt aggregates, and subsequently combining these with NPs to form the hollow sphere structures. Stucky and co-workers recently reported a similar materials synthesis approach.[34] The spheres are nominally in the 1−4 micron diameter range, the

---

* To whom correspondence should be addressed. Tel: +1-713-348-3511. Fax: +1-713-348-5478. E-mail: mswong@rice.edu.
  † Department of Chemical and Biomolecular Engineering.
  ‡ Department of Chemistry.
  § Current address: Indian Institute of Chemical Technology, Tarnaka, Hyderabad, AP, India 500007.

shell walls are made of NPs and polymer, and the core interior can contain either water or polymer. These spheres are called nanoparticle-assembled capsules, or NACs. The "hollow sphere" and "capsule" terms are used interchangeably, with "polymer-filled" and "water-filled" referring to the contents of the core. This synthesis is rapid and scalable, and it occurs under ambient conditions, in water, and at mild pH values. NAC synthesis further allows the nondestructive encapsulation of water-soluble compounds. Thus, NP assembly offers new possibilities for engineering microcapsules for encapsulation applications, relative to the preparation methods of self-assembly, sacrificial templating, and physical formation.

In this paper, we primarily focus on understanding the noncovalent chemistry involved in the first step of NAC synthesis, namely, the formation of polymer−salt aggregates. We use poly(allylamine hydrochloride) (PAH) as the model cationic polyelectrolyte, to study its aggregation behavior as induced by multivalent anions as a function of charge ratio, pH, and aging time. We discuss the electrostatic interactions between PAH and anions in terms of counterion condensation and discuss the growth of the PAH−salt aggregates in terms of charged colloid stability. Finally, we analyze the effect of polymer aggregate aging time on NAC size. The NACs studied in this work are polymer-filled, and not water-filled, microcapsules.

Experimental Section

Materials. PAH (70 000 g/mol, chloride counterion), tetrasodium ethylenediaminetetraacetate (98%, "EDTA"), disodium citrate (98%), monosodium citrate (99%), and sodium acetate (99.8%) (all from Sigma-Aldrich), as well as trisodium citrate ("cit") and disodium sulfate (99+%) (both from Fisher Scientific) were used as received. Polyelectrolyte stock solution and all subsequent diluted precursor solutions were made using deionized water (18.2 MΩ, Barnstead Nanopure Diamond System). Glutaraldehyde (25% aqueous solution, Sigma-Aldrich) was used as received. The fluorescent dyes of fluorescein isothiocyanate (FITC) and rhodamine B isothiocyanate (RITC) were procured from Sigma-Aldrich. SiO_2 NPs (Snowtex-O, Nissan Chemicals) were available as an aqueous colloidal suspension (20.5 wt %, pH 3.4, ionic strength $I = 16.9$ mM). The NPs measured 13 ± 3 nm in diameter, according to dynamic light scattering. The zeta potential of the SiO_2 NPs in the original sol condition was calculated from their electrophoretic mobility $(-1.4 \ (\mu m/s)/V/cm))$ to be -16 mV in the Henry's limit.

Synthesis. All experiments with polyelectrolyte−salt solutions were done at a specific charge ratio R, which is defined as the ratio of total negative charge of the added salt to the total positive charge of the polymer ($R = $ [anion] $\times |z_-|/$ [polymer] $\times |z_+|$, where z_- is the negative charge per anion and z_+ is the positive charge per chain). A typical preparation of a PAH−cit suspension was carried out by combining 1 mL of PAH precursor solution (precursor concentration range of 0.01 to 40 mg/mL) with 2.5 mL of cit solution (precursor concentration range of 1.4×10^{-2} to 71.3 mM) in a polystyrene centrifuge tube, resulting in a final PAH concentration of 2.9×10^{-3} to 11.4 mg/mL. Immediately, the resulting aliquot became turbid, except in cases of low PAH precursor concentration (≤ 0.1 mg/mL) in which turbidity was not apparent by eye. This turbid reaction mixture was vortex-mixed for 10 s at low a speed (5 speed on a 1−10 scale, Fisher Scientific Mini Vortexer); the aging time of the suspension started at the end of mixing. The NACs were prepared by adding 2.5 mL of the stock SiO_2 NP sol to the above polymer−salt suspension (aged for 30 min) and vigorously vortex-mixing at 7 speed for 20 s.

PAH−FITC and PAH−RITC stock solutions (50 mg/mL) were prepared in water and refrigerated (Supporting Information). The average number of dye molecules per PAH chain was ∼2, as determined through fluorescence spectroscopy.

Characterization. *Atomic Force Microscopy (AFM).* Tapping-mode AFM was performed on a Digital Instrument Nanoscope IIIA atomic force microscope using a 125 micrometer TESP tip. After aging for 30 min, 100 μL of a prepared suspension (1 mL of PAH solution (5 mg/mL) + 2.5 mL of cit solution (14.26 mM, $R = 2$)) was placed on a freshly cleaved mica surface. After 1 min of deposition time, the mica substrate was rinsed with deionized water and dried overnight (∼12 h) before imaging.

Chloride Ion Selective Electrode Measurements. Potentiometric measurements for detecting free chloride ions were performed using a Thermo Orion model 720A Plus bench-top meter and a chloride Ionplus electrode (Orion Cat. No. 9617BN) at room temperature. Each measurement was taken immediately after sample preparation, lasting ∼1 min. The free chloride concentration was measured for PAH−salt suspensions in the range of $R = 0.1-10$. Measurements were inaccurate above $R = 5$ for the PAH−EDTA case due to high ionic strength effects. Three-point calibration was performed using NaCl solutions (100, 10, and 1 mM).

Cryo-Transmission Electron Microscopy (Cryo-TEM). TEM was performed on a JEOL 2010 FasTEM system at a 100 kV electron beam accelerating voltage. 1 mL of PAH solution (0.1 mg/mL) was combined with 2.5 mL of cit solution (0.713 mM, $R = 5$) and vortex-mixed for 10 s. Immediately afterward, a drop of the suspension was cast onto a holey carbon copper TEM grid, followed by vitrification in liquid ethane. The grid was then transferred to liquid nitrogen and stored (for approximately 30 min) until imaging.

Dynamic Light Scattering (DLS). Size distribution analysis was carried out with Brookhaven ZetaPALS DLS equipment with a BI-9000AT digital autocorrelator at 656 nm wavelength. All studies were done at a 90° scattering angle and temperature controlled at 25 °C in standard 4 mL polystyrene cuvettes.

For studying the evolution of PAH−salt aggregates with time, size measurements were taken of suspensions using the software package "9KPSDW." Measurements began 3 min after vortex-mixing and were carried out for a total of 30 min, with each consecutive run (as one data point) lasting for 2 min. The 3-min time gap was due to transferring the suspension from the synthesis tube to the DLS cuvette and instrument setup.

Electrophoretic Mobility Analysis. Electrophoretic mobility was measured by phase analysis light scattering (PALS) in the Brookhaven ZetaPALS setup. A dip-in (Uzgiris-type) electrode system with 4 mL polystyrene cuvettes was used, and measurements were taken at 25 °C.

Laser Scanning Confocal Microscopy. Confocal images were captured with a Carl Zeiss LSM 510 inverted microscope equipped with a $100\times$ oil immersion objective (NA = 1.4). A laser excitation wavelength of 488 nm was chosen for FITC ($\lambda_{ex} = 494$ nm, $\lambda_{em} = 519$ nm), and an excitation wavelength of 543 nm was chosen for RITC ($\lambda_{ex} = 560$ nm, $\lambda_{em} = 580$ nm). Samples were mounted on conventional glass slides and sealed under a cover slip to prevent drying. All samples were prepared approximately 0.5−1 h prior to imaging. For two-color simultaneous imaging, it was confirmed (by confocal microscopy and fluorescence spectroscopy) that there was negligible emission spectrum overlap between the two dyes.

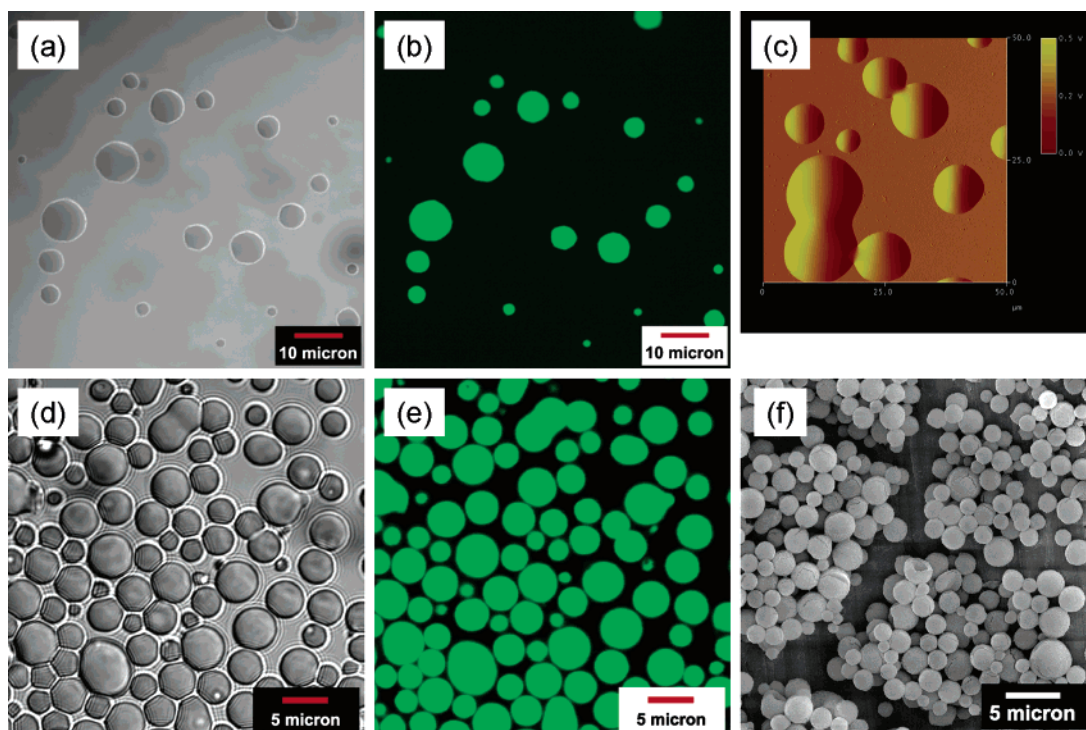*Scanning Electron Microscopy (SEM).* SEM was carried out in a JEOL6500 field emission microscope equipped with an

Nanoparticle-Assembled Capsule Synthesis

J. Phys. Chem. B, Vol. 110, No. 51, 2006 **25621**

Figure 1. (a) Bright-field and (b) confocal microscopy images of surface-bound PAH−FITC−cit aggregates in a water environment. (c) AFM images of air-dried PAH−cit aggregates supported on freshly cleaved mica surface. Synthesis conditions: [PAH]$_{final}$ = 1.43 mg/mL, [cit]$_{final}$ = 10.19 mM, $R = 2$, aging time of PAH−cit suspension = 30 min. (d) Bright-field, (e) confocal microscopy, and (f) SEM images of the resultant capsules after the addition of SiO$_2$ NPs to the above PAH−cit suspension.

in-lens thermal field emission electron gun. A secondary electron image was taken at a 15 kV electron beam with a working distance of 10.0 mm. The microcapsule suspension was aged for one week, washed with water, and loaded on an SEM stub. After drying overnight, the sample was sputter-coated with gold.

Results and Discussions

Morphology of PAH−cit Aggregates. A clear PAH−FITC solution (5 mg/mL) immediately turned turbid when combined with a cit solution ($R = 2$), indicating the formation of light-scattering PAH−cit aggregate domains. After aging for 30 min, the PAH−cit suspension was imaged through optical microscopy (Figure 1a,b). Adhering to the glass coverslip, the aggregates were 1−8.5 μm in size and were homogeneously fluorescent, indicating that they were composed of PAH−FITC. The addition of silica NPs to the PAH−cit suspension-containing reaction tube led to the formation of microcapsules with NP/polymer shell walls and polymer-filled cores (Figure 1d−f). The confocal image showed that the polymer distributions for different particles were two-dimensionally uniform at a given focal plane, which supports the three-dimensional uniformity of polymer distribution within polymer-filled NAC particles (Figure 1e).

Under dried conditions during AFM measurement, the aggregates were dome-shaped, indicating a flattening of the spherical aggregates (Figure 1c). The wide range in dried aggregate height (100−800 nm) and the deviation from the hydrodynamic diameter of the aggregate suspension (2.7−3.8 μm) are the result of uncontrolled aggregate spreading across the mica surface and evaporative loss of internal water. High-resolution scanning of a small surface area of the domains (50 × 50 nm^2 area, data not shown) showed a smooth surface devoid of any notable surface features at a height resolution of 10 nm, suggesting a compact packing of the dried polymer−salt aggregate.
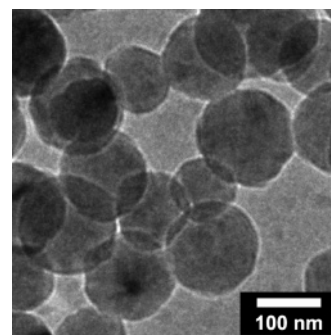

Figure 2. Cryo-TEM image of PAH−cit aggregate suspension. Synthesis conditions: [PAH]$_{final}$ = 0.029 mg/mL, [cit]$_{final}$ = 0.2 mM, $R = 2$, no aging of PAH−cit suspension.

Cryo-TEM was used to capture aggregate morphology in suspension and to eliminate surface spreading effects. Dilute solutions of the precursors and no aging aided in the imaging of small aggregates (Figure 2). The clusters were spherical, ranging in size from 70 to 210 nm. The average diameter was measured to be 120 nm, and the standard deviation was found to be 45 nm (based on >175 aggregates).

We note that others have recently reported similar experimental observations in which polyamines formed aggregates in the presence of multivalent anions.[35−38] Kröger et al. reported that the cationic polypeptides isolated from diatom cell walls formed polymer aggregates if the polymer carried covalently bound phosphate groups or if a phosphate buffer was used.[38] Patwardhan and Clarson remarked that PAH was "not fully soluble in phosphate−citrate buffer" in their study on silica synthesis.[35]

Charge Ratio R Effect on PAH−Salt Aggregate Formation. At very low R ratios, the addition of small amounts of monovalent (acetate), divalent (succinate), trivalent (cit), or tetravalent (EDTA) salt negligibly increased the free Cl
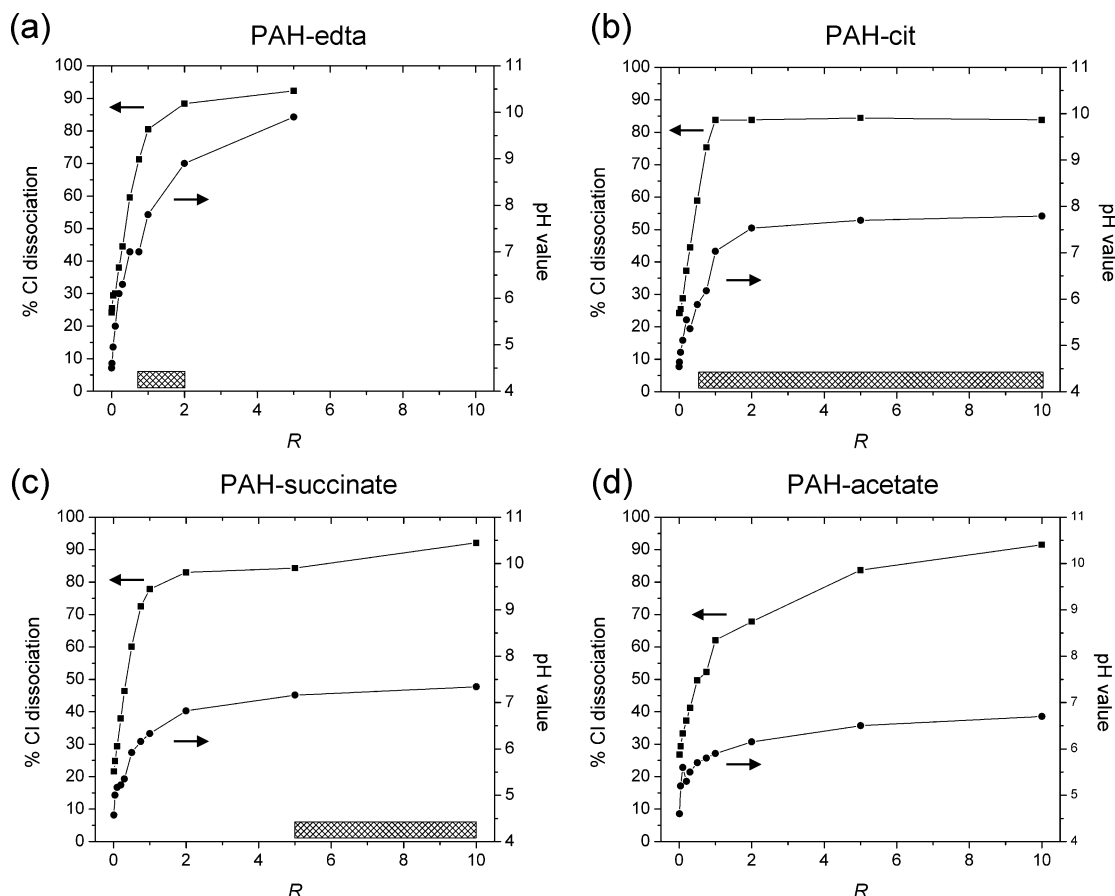
Figure 3. Percentage of total Cl in PAH solution as free ions (squares) and corresponding pH values (circles) as a function of charge ratio for multivalent salts: (a) EDTA, (b) cit, (c) succinate, and (d) acetate. Hatched marks indicate the *R* values at which aggregate formation occurred. Synthesis: [PAH]$_{final}$ = 1.43 mg/mL, no aging.

concentration (Figure 3). Above $R = 0.01$, the free Cl concentration increased for the four salts. PAH aggregation was observed for all salts, except for the acetate anion (Figures 1b and S1 (Supporting Information)).

We consider the process of salt-induced PAH aggregate formation to proceed with counterion condensation[39] followed by aggregation of the polyelectrolyte chains.[40−42] For polyelectrolyte solutions, it is well-known through the Manning theory on counterion condensation that a fraction of the polymer counterions are bound or condensed onto the polyelectrolyte backbone in order to reduce the electrostatic repulsion energy of adjacent charged polymer units ($e^2/4\pi\epsilon b$) relative to thermal energy levels (k_BT).[39,43] ϵ is the dielectric constant of pure bulk solvent, k_B is the Boltzmann constant, T is the absolute temperature, and b is the length of a polymer unit. The Manning theory provides a starting point as a simple theoretical model for understanding counterion condensation and polyelectrolyte solution behavior.[39]

The Manning parameter is given as $\xi = l_B/b$, where l_B is the Bjerrum length ($= e^2/4\pi\epsilon k_BT$), which represents the effective distance between charged polymer units at which electrostatic energy equals thermal energy. The Bjerrum length in water at 25 °C is 7.14 Å. If the ξ value of a polyelectrolyte solution is calculated to be >1, then counterion condensation is expected. For a PAH solution ($b = 3.8$ Å, estimated from Chem3D) at 25 °C, we calculated ξ to be 1.89 and the percentage of Cl as condensed ions to be $1 - (1/\xi) = 47\%$.[39] By measuring the free Cl concentration of a PAH solution (5 mg/mL), we determined that 75% of the total Cl content was bound to the PAH backbone, clearly demonstrating Cl condensation (Figure 3). The discrepancy between the predicted and measured values

is attributed to oversimplifications in the Manning theory; for example, the polymer molecule is modeled as an infinitely long and infinitely thin chain of point charges separated by distance b, and there are no interactions among polymer chains.[44]

As determined from the low R regime ($R < 1$), 1.8, 1.5, 1.0, and 0.3 Cl anions were displaced per molecule of EDTA, cit, succinate, and acetate, respectively. The maximum Cl displacement was in the range of 80−90% up to salt concentrations of $R = 10$. One hundred percent Cl dissociation is not expected, due to incomplete substitution of monovalent counterions by the multivalent ones.[44,45]

It is helpful to consider multivalent anions as ionic cross-linkers between the polymer chains due to their multiple negatively charged carboxylate "binding sites,"[33] of which the acetate anion has only one binding site. We presume that specific ion-pair site-binding occurs (e.g., carboxylate and ammonium salt bridges in polycarboxylate−polyammonium complexes).[46−49] The electrostatic interaction may be nonspecific also, in that the ions are bound to, but delocalized about, the polyelectrolyte chain.[50]

Characterized by an immediate 10-fold increase in scattering intensity according to DLS, multivalent salt-cross-linked polymer aggregates were formed once a "critical" charge ratio R_c was reached (Figure 3). The R_c values for EDTA and cit were less than 1 (0.75 and 0.6, respectively), indicating that a one-to-one charge stoichiometry was not required for aggregation to occur. It is not clear, though, why the R_c for divalent succinate was >1. For comparison, divalent sulfate was found to have an R_c of 0.75 (Figures S1b and S2, Supporting Information), indicating that anion molecular structure has a strong effect on R_c.
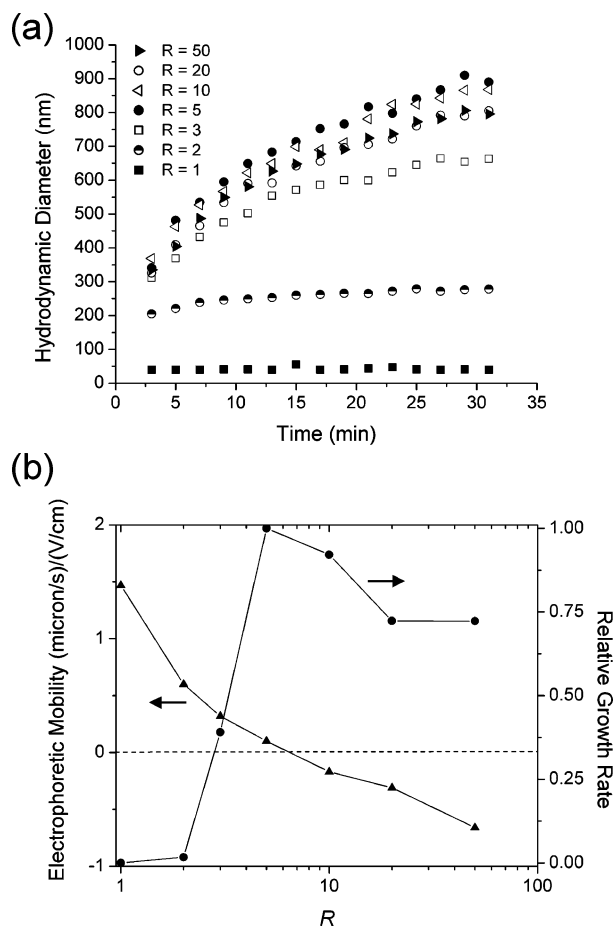
Figure 4. (a) Hydrodynamic diameter−time curves and (b) electrophoretic mobility and relative growth rates of PAH−cit aggregates as a function of R. Synthesis: $[PAH]_{final} = 0.029$ mg/mL.

In the case of the PAH−EDTA system, there was an upper critical charge ratio ($R = 2$), above which aggregate formation did not occur. This was due to the high suspension pH resulting from the use of the tetrasodium form of EDTA. Above $R = 2$, pH was greater than 9.0, which exceeded the pK_a of the protonated amine group of PAH ($\sim 8.5^{51}$). The very high pH value "turned off" the positive charge of the polymer, thereby removing the electrostatic driving force between the EDTA and PAH.

Charge Ratio R Effect on PAH−Salt Aggregate Growth Rate. PAH−cit aggregates had growth rates that were dependent on charge ratios (Figure 4a). Aggregation was observed at R_c = 0.8, which was slightly higher than the R_c = 0.6 value indicated earlier, due to the lower final PAH concentration used (0.029 mg/mL versus 1.43 mg/mL; Figure S3, Supporting Information). The lower polymer concentration was needed to reduce aggregate growth rates so that relative growth rates could be calculated accurately.

The aggregate growth rate increased from near-zero at R = 1 to a maximum at R = 5, decreased above R = 5, and leveled off at 75% of the maximum growth rate at R = 20 (Figure 4b). To understand this growth rate dependence on R, we characterized the polymer aggregate surface charge via electrophoretic mobility (μ_E) measurements. Calculated from the measured velocity v of the charged colloids in an applied external electric field ($E = \mu_E \times v$), electrophoretic mobility reflects the overall charge of a colloidal surface and surface-bound counterions. The large μ_E values of the PAH−cit aggregates at low R ratios indicated the aggregate surface was highly positively charged (Figure 4b). As the R ratios increased, the surface charge became

less positively charged until about R = 5, at which point the aggregates had an overall neutral surface charge. Above R = 5, the aggregates assumed a net negative charge, arising from citrate anions binding to the surface.

We found that the growth rate of the PAH aggregates could be correlated to their surface charge, by treating the aggregates as charged colloidal particles. According to the DLVO theory of colloidal stability, charged particles are most susceptible to aggregation when their surfaces are the least charged or, equivalently, when the van der Waals attractive energy between the particles overcomes the repulsive energy of the charged surfaces.[52,53] Thus, it stood to reason that PAH aggregates had slow growth rates at low R ratios because their surfaces were charge stabilized against aggregation. The aggregate growth rate increased with higher R ratios as the surface charge reduced in magnitude and reached a maximum when the net surface charge was nearly zero (Figure 4b).

The growth rate then decreased as the aggregate surface became negatively charged. Higher R ratios led to a more negatively charged surface, but the growth rate did not decrease above R = 20. The presence of free, unbound citrate anions may have been responsible for these high growth rates by increasing the overall salt concentration of the suspension, as high salt concentrations are known to reduce the electrostatic repulsion between charged particles (which leads to colloid destabilization).[54]

pH Effect on PAH−Salt Aggregate Formation. We studied the pH effect at constant salt concentration by using the three different sodium salts of citrate (trisodium, disodium, monosodium) and citric acid, and preparing PAH−cit samples at R = 5 and low polymer concentrations. All the salt forms led to aggregate formation (Figure 5a, curves i, iii, and iv). Citric acid did not though, as the scattering intensity of the citric acid−PAH solution was only slightly higher than that of a pure PAH solution and was similar to that of a PAH solution containing NaCl (Figure 5b, samples v−vii).

The measured pH values of the PAH−cit solutions/suspensions were 7.4, 5.3, 3.9, and 3.4 for the tri-, di-, monosodium, and citric acid samples, respectively, which indicated that pH affected the ability of polymer aggregates to form. We propose that the pH of the PAH−cit suspension dictated the ionic state of the citrate anion and therefore the population of multicharged anions. Citric acid has pK_a values of 3.14, 4.77, and 6.39, resulting in a distribution of differently charged citrate species as a function of solution pH (Figure 5c). According to acid−base equilibrium calculations, the citrate anions were mostly in the form of trivalent cit^{3-} species when the trisodium salt was used and in the form of divalent $Hcit^{2-}$ for the disodium salt (Figure 5d). When the monosodium citrate was used, the citrate anions were mostly monovalent H_2cit^-, but $\sim 10\%$ were in divalent form. Thus, the formation of aggregates correlated with the presence of 2- and 3- charged citrate species.

In contrast to those in the PAH−trisodium citrate case, the PAH−disodium citrate aggregates grew very slowly over time. The aggregate hydrodynamic diameter was 110 nm, according to DLS. To verify their existence, we aged the suspension for 30 min and treated them with glutaraldehyde to form covalently cross-linked aggregates that could be imaged outside the water suspension. SEM analysis indicated that the aggregates were ~ 100 nm spheres (Figure S4, Supporting Information). The PAH−monosodium citrate aggregates also did not grow with time. The scattering intensity of this suspension was significantly less than that of the PAH−disodium citrate case but higher than that of a PAH solution (Figure 5b). The measured D_h of ~ 25
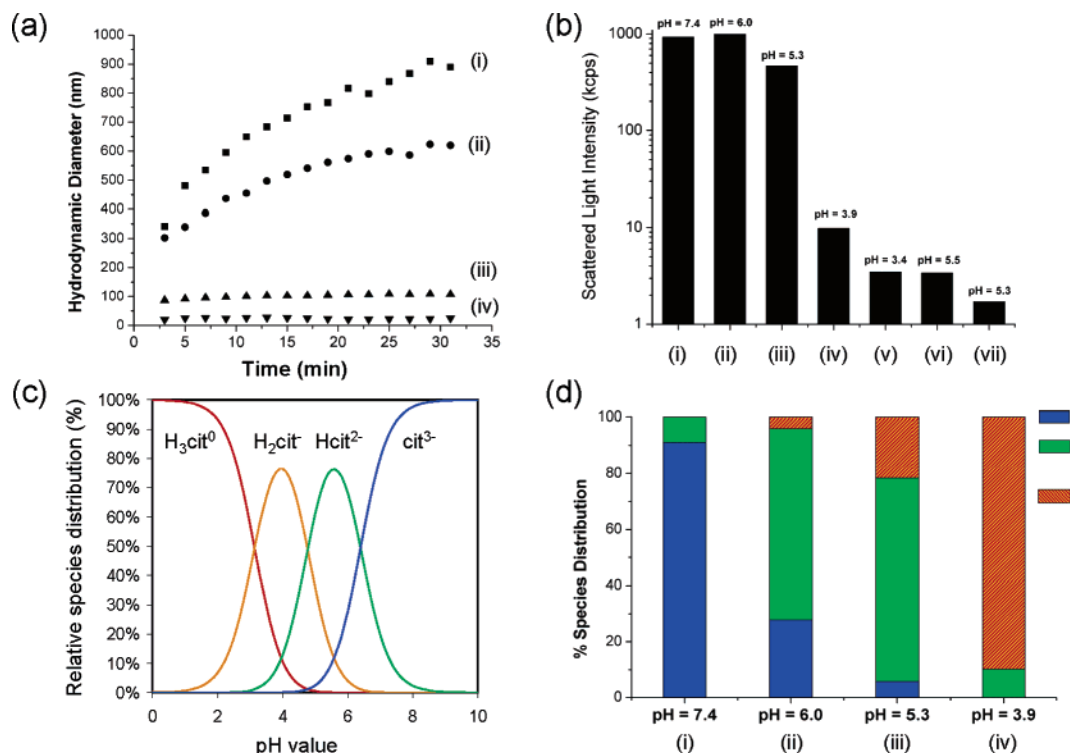
Figure 5. Effect of suspension pH on PAH−cit aggregate growth using different salts ([PAH]$_{final}$ = 0.029 mg/mL, [cit]$_{final}$ = 0.51, R = 5): (a) aggregate size as a function of aging time, (b) scattered light intensity (log-scale) of the different PAH−cit systems, (c) citrate species distribution calculated as a function of pH, and (d) the calculated species distribution at the pH values of PAH−cit systems shown in panel a. The samples were prepared using (i) trisodium citrate, (ii) 50% trisodium citrate + 50% disodium citrate, (iii) disodium citrate, (iv) monosodium citrate, (v) citric acid, (vi) NaCl (R = 5), and (vii) no salt.

nm suggested the presence of stable PAH−cit aggregates composed of ∼8−9 PAH chains.

The aggregate growth rates varied as a function of pH value (Figure 5a). Electrophoretic mobility measurements of the faster-growing PAH−trisodium citrate (pH 7.4) and slower-growing PAH−disodium citrate (pH 5.3) suspensions yielded μ_E values of +0.09 and +0.48 (μm/s)/(V/cm), respectively. The (fast growth rate)/(low surface charge) and (slow growth rate)/(high surface charge) observations were thus consistent with the earlier explanation for the R effect on growth rate. As expected, an equimolar solution of disodium citrate and trisodium citrate (pH 6.0) led to PAH−cit aggregate formation with an intermediate μ_E value (+0.37 (μm/s)/(V/cm)) and an intermediate growth rate (Figure 5a, curve ii). The μ_E value for the nongrowing, higher-pH, PAH−monosodium citrate system (pH 3.9) was expected to be greater than +0.48 (μm/s)/(V/cm), but it could not be determined accurately due to low scattering intensity.

PAH−cit Aggregate Growth Mechanism. PAH−cit aggregates were found to grow in size while maintaining their spherical shape, as visualized through confocal microscopy of FITC-tagged PAH−cit (Figure 6a−c) and RITC-tagged PAH−cit aggregates as a function of aging time (Figure 6f−h). The growth mechanism was unclear, though. Therefore, separate suspensions of FITC-tagged PAH−cit and RITC-tagged PAH−cit aggregates were prepared and aged for 19 min. They were combined, aged for 1 min, and imaged. The suspension was found to comprise small aggregates (<3 μm), which mostly contained either FITC (green) or RITC (red), and larger aggregates (>3 μm) that contained mixtures of the two dyes (Figure 6d). A longer aging time led to aggregates that were larger and more homogeneous in composition (Figure 6e). These images indicated that aggregate growth could have been the result of coalescence, in which the aggregates merge to form
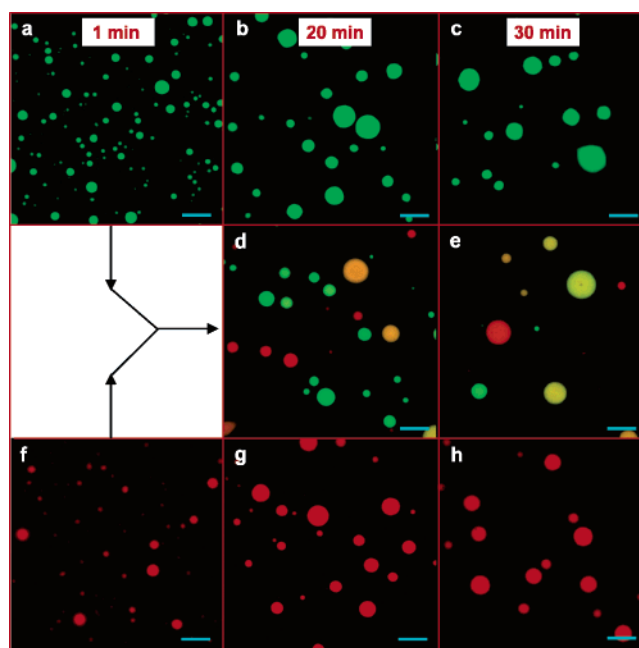

Figure 6. Confocal microscopy images of PAH−cit aggregates aged for various times (1, 20, and 30 min): FITC-tagged PAH−cit aggregates aged for (a) 1 min, (b) 20 min, and (c) 30 min; RITC-tagged PAH−cit aggregates aged for (f) 1 min, (g) 20 min, and (h) 30 min; and the resultant aggregates after combining the 19-min-aged FITC- and RITC-tagged suspensions from panels a and f, respectively, and aging for (d) 1 min and (e) 11 min. Synthesis: [PAH]$_{final}$ = 1.43 mg/mL, [cit]$_{final}$ = 10.19 mM, R = 2. Scale bars: 10 μm.

larger aggregates, or Ostwald ripening, in which larger aggregates grow while the smaller ones dissolve.

We tested the hypothesis that the aggregates grew through coalescence, by examining the effect of PAH concentration on
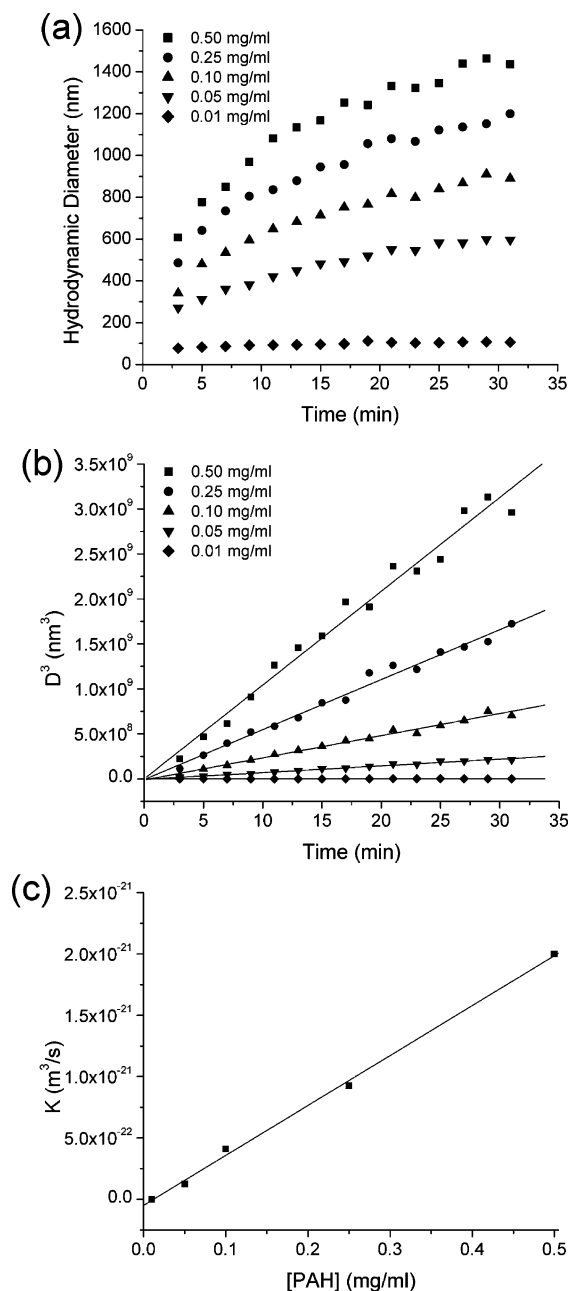
Nanoparticle-Assembled Capsule Synthesis

J. Phys. Chem. B, Vol. 110, No. 51, 2006 **25625**

Figure 7. PAH−cit aggregate growth as a function of PAH precursor concentration: (a) D_h vs time, (b) D_h^3 vs time, and (c) rate constant vs polymer concentration. The highest precursor PAH concentration tested was 0.50 mg/mL, due to multiple scattering of the PAH−cit suspensions at higher PAH concentrations. Synthesis: $[PAH]_{final} = [PAH]_{precursor} \div 3.5$; $R = 5$.

D_h−time curves at constant R. On the basis of the treatment developed for polymer melt systems by Crist and Nesarikar,[55] spherical droplets with diameter D grow via coalescence or Ostwald ripening with a cube-root time dependence, $D^3 = D_0^3 + Kt$, where D_0 is initial diameter and K is a growth mechanism-dependent rate constant. It was shown that $K \propto \phi$ for coalescence and $K \propto 1/(1 + 0.74\sqrt{\phi})^3$ for Ostwald ripening, where ϕ is the total volume fraction of the droplets in suspension.

The PAH−cit aggregates were found to grow more rapidly at higher PAH concentrations (Figure 7a). It could be seen that the D_h^3−time curves were linear, allowing for reasonably accurate K estimates (Figure 7b). The curves extrapolated to a common D_0 value of 80 nm, which suggested a common PAH−cit aggregate size after the 10-s vortex-mixing step. With the assumption that the volume fraction of PAH−cit aggregates was
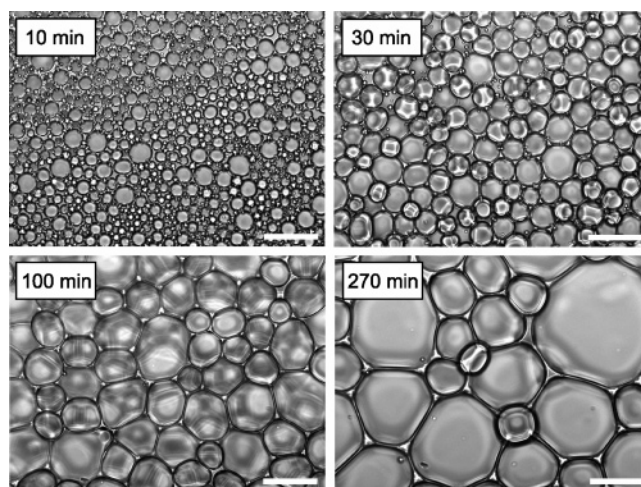

Figure 8. Time-lapse bright-field microscopy images of concentrated PAH−cit aggregate "droplets." The field of view did not change. Time zero corresponds to when the 10-s vortex-mixing stopped. Synthesis: $[PAH]_{final} = 11.43$ mg/mL, $[cit]_{final} = 50.9$ mM ($R = 1.2$). Scale bar: 50 μm.

proportional to the initial PAH concentration, the observation that the K rate constants increased linearly with PAH concentration (Figure 7c) strongly suggested the coalescence growth mechanism.

Real-time studies on PAH−cit aggregate growth through optical microscopy provided additional evidence for coalescence. A concentrated PAH−cit suspension was made by adding 125 μL of Na₃cit solution (71.3 mM, $R = 1.2$) to 50 μL of PAH solution (40 mg/mL) and vortex-mixing for 10 s. A drop of the highly turbid suspension was deposited on a glass slide and left sitting for 2 min, and excess suspension was lightly rinsed with water.[56] The high PAH concentration ensured a dense packing of aggregates on the glass slide, which was difficult to prepare using lower PAH concentrations. The glass slide-bound aggregates appeared as droplets at early times (Figure 8a). They deformed upon contact with one another and underwent coalescence very slowly (Figure 8b−d). This coalescence behavior is reminiscent of surfactant-containing oil-in-water emulsions:[54,57,58] (i) droplets approach one another and deform; (ii) the liquid film between the flat surfaces of the droplets starts draining; (iii) the surfaces make physical contact and fuse to form a neck; and (iv) the neck grows such that the two droplets re-form into a spherical droplet. PAH−cit aggregate coalescence may be slow due to the charged nature of the droplet surface. We then probed the existence of Ostwald ripening by depositing PAH−cit aggregates (same concentrations as above) on a glass slide at a low surface density such that there was no droplet−droplet contact (Figure S5, Supporting Information).[59] We did not observe any of the change in aggregate size expected for Ostwald ripening.

Effects of PAH−cit Aggregate Aging Time and R Ratio on Capsule Size. The formation of the NAC shell depended on the R ratio of the PAH−cit samples (Figure S6, Supporting Information). After SiO₂ NP sol addition, disordered silica/polymer precipitate resulted at $R = 0$ and $R = 0.3$, since no PAH−cit aggregates were formed below the critical R ratio of 0.6. Silica/polymer microcapsules, on the other hand, resulted for R ratios greater than the critical R ratio. No obvious morphological differences in the NACs synthesized at the different R values were observed. The capsules were formed whether the electrophoretic mobilities were positive or negative in value, reinforcing the fact that electrophoretic mobility
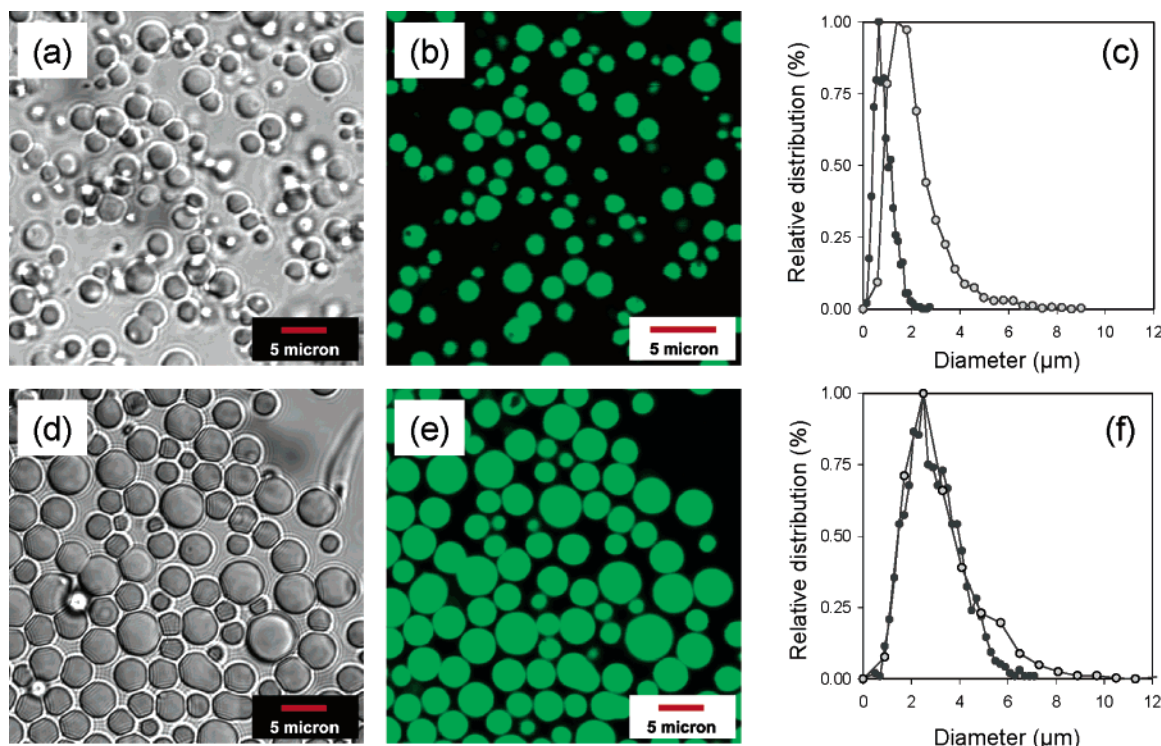
Figure 9. Bright-field and confocal microscopy images of NACs prepared from PAH−FITC−cit aggregates aged for 10 s (a,b) and 30 min (d,e). (c,f) Size distributions of PAH−cit aggregates (filled circles) aged for 10 s and 30 min, respectively, and the resultant NACs (open circles). $[PAH]_{final}$ = 0.83 mg/mL, $[cit]_{final}$ = 5.94 mM, $[SiO_2\ NP]_{final}$ = 8.5 wt %, aging time after NP addition = 30 min.

measurements provide only average values and do not account for the charge heterogeneity of the surface.

Finally, we studied the effect of PAH−cit aggregate aging time on microcapsule size (Figure 9). On the basis of SEM analysis of more than 1000 glutaraldehyde-treated PAH−cit aggregates, they had a mean diameter of 0.85 μm (standard deviation σ = 0.38 μm) after aging for 10 s, and a mean diameter of 2.93 μm (σ = 1.10 μm) after aging for 30 min (Figure 9c,f). The polymer aggregates broadened in size with aging time. The addition of SiO_2 NPs to 10-s-aged and 30-min-aged aggregates led to NACs with mean diameters of 2.1 μm (σ = 1.1 μm) and 3.3 μm (σ = 1.8 μm), respectively. The capsule structures were similar (i.e., spherical shell shape and core interior contained polymer), and the NAC sizes correlated to aggregate aging time.

The relationship between NAC and aggregate diameters was less clear. For the 10-s-aged system, the difference in aggregate and NAC diameters suggested a shell thickness of 600 nm, which is larger than the 100−250 nm thicknesses typically observed in PAH-based NACs (Figure S7, Supporting Information).[33] For the 30-min-aged system, the difference in diameters suggested a shell thickness of 200 nm. This calculation may be misleading, as the size distributions of the aggregates and NACs mostly coincided, but the positive skew of the size distribution led to a larger NAC mean diameter. A detailed study of the shell formation step and the NAC structure is ongoing.

Conclusions

The room-temperature formation of PAH−salt aggregates is readily performed by mixing the respective solutions together at appropriate charge ratio R and pH values. To the first approximation, the formation can be understood on the basis of electrostatic attractions between positively charged PAH and multiply charged anions and electrostatic interactions between the charged PAH−salt aggregates. The anions bind to the PAH

backbone via counterion condensation, and the resulting PAH−salt complexes combine to form colloidal aggregates. These aggregates grow as a function of time, with the growth rates being dependent on their surface charge. The coalescence mechanism for aggregate growth is supported by DLS measurements and optical studies of concentrated PAH−cit aggregate suspensions that resemble emulsions. The polymer aggregates behave as soft templates for NACs formation, such that aggregate aging time controls capsule diameter. This fuller understanding of the electrostatic chemistry involved in polymer aggregate formation is important in controlling microcapsule structure, and should be helpful in understanding the formation of other charge-assembled materials, such as DNA−salt aggregates and complex coacervates.

Supporting Information Available: Experimental methods along with the following figures: Figure S1: Confocal microscopy images of aggregates formed from PAH and various multivalent salts. Figure S2: Percentage of total Cl in PAH solution as free ions and corresponding pH values as a function of charge ratio for sulfate salt. Figure S3: Critical R values plotted against polymer concentration for the PAH−cit system. Data points were collected by visual inspection and laser light scattering. Figure S4: SEM image of spheres formed by the addition of glutaraldehyde to PAH−disodium citrate aggregates. Figure S5: Time-lapse differential interference contrast images of PAH−cit aggregates (low coverage of glass slide). Figure S6: Optical microscopy images of product formed after com-

bining SiO$_2$ NPs with PAH−cit samples of varying R ratios. Figure S7: SEM image of an ultramicrotomed capsule. This material is available free of charge via the Internet at http://pubs.acs.org.

References and Notes

(1) Philippot, J. R.; Schuber, F. *Liposomes as Tools in Basic Research and Industry*; CRC Press: Boca Raton, FL, 1995.

(2) Wilcox, D. L., Sr.; Berg, M.; Bernat, T.; Kellerman, D.; Cochran, J. K., Jr. *Hollow and Solid Spheres and Microspheres: Science and Technology Associated with Their Fabrication and Application*; Materials Research Society: Pittsburgh, PA, 1995.

(3) Gibbs, B. F.; Kermasha, S.; Alli, I.; Mulligan, C. N. *Int. J. Food Sci. Nutr.* **1999**, *50*, 213.

(4) Uludag, H.; De Vos, P.; Tresco, P. A. *Adv. Drug Delivery Rev.* **2000**, *42*, 29.

(5) Barenholz, Y. *Curr. Opin. Colloid Interface Sci.* **2001**, *6*, 66.

(6) Chah, S.; Fendler, J. H.; Yi, J. *J. Colloid Interface Sci.* **2002**, *250*, 142.

(7) Yang, M.; Ma, J.; Zhang, C.; Yang, Z.; Lu, Y. *Angew. Chem., Int. Ed.* **2005**, *44*, 6727.

(8) Caruso, R. A.; Antonietti, M. *Chem. Mater.* **2001**, *2001*, 3272.

(9) Cochran, J. K. *Curr. Opin. Solid State Mater. Sci.* **1998**, *3*, 474.

(10) Vriezema, D. M.; Hoogboom, J.; Velonia, K.; Takazawa, K.; Christianen, P. C. M.; Maan, J. C.; Rowan, A. E.; Nolte, R. J. M. *Angew. Chem., Int. Ed.* **2003**, *42*, 772.

(11) Discher, B. M.; Won, Y. Y.; Ege, D. S.; Lee, J. C.; Bates, F. S.; Discher, D. E.; Hammer, D. A. *Science* **1999**, *284*, 1143.

(12) Jenekhe, S. A.; Chen, X. L. *Science* **1998**, *279*, 1903.

(13) Douglas, T.; Young, M. *Nature* **1998**, *393*, 152.

(14) Takeda, N.; Umemoto, K.; Yamaguchi, K.; Fujita, M. *Nature* **1999**, *398*, 794.

(15) Kawahashi, N.; Matijevic, E. *J. Colloid Interface Sci.* **1990**, *138*, 534.

(16) Zhong, Z. Y.; Yin, Y. D.; Gates, B.; Xia, Y. N. *Adv. Mater.* **2000**, *12*, 206.

(17) Liu, S.; Zhang, Z.; Han, M.-Y. *Adv. Mater.* **2005**, *17*, 1862.

(18) McKelvey, C. A.; Kaler, E. W.; Zasadzinski, J. A.; Coldren, B.; Jung, H. T. *Langmuir* **2000**, *16*, 8285.

(19) Dinsmore, A. D.; Hsu, M. F.; Nikolaides, M. G.; Marquez, M.; Bausch, A. R.; Weitz, D. A. *Science* **2002**, *298*, 1006.

(20) Hsu, M. F.; Nikolaides, M. G.; Dinsmore, A. D.; Bausch, A. R.; Gordon, V. D.; Chen, X.; Hutchinson, J. W.; Weitz, D. A. *Langmuir* **2005**, *21*, 2963.

(21) Donath, E.; Sukhorukov, G. B.; Caruso, F.; Davis, S. A.; Möhwald, H. *Angew. Chem., Int. Ed.* **1998**, *37*, 2202.

(22) Caruso, F. *Adv. Mater.* **2001**, *13*, 11.

(23) Wang, Y.; Yu, A.; Caruso, F. *Angew. Chem., Int. Ed.* **2005**, *44*, 2888.

(24) Angelatos, A. S.; Radt, B.; Caruso, F. *J. Phys. Chem. B* **2005**, *109*, 3071.

(25) Schacht, S.; Huo, Q.; Voigt-Martin, I. G.; Stucky, G. D.; Schüth, F. *Science* **1996**, *273*, 768.

(26) Marinakos, S. M.; Novak, J. P.; Brousseau, L. C.; House, A. B.; Edeki, E. M.; Feldhaus, J. C.; Feldheim, D. L. *J. Am. Chem. Soc.* **1999**, *121*, 8518.

(27) Jiang, P.; Bertone, J. F.; Colvin, V. L. *Science* **2001**, *291*, 453.

(28) Schmidt, H. T.; Ostafin, A. E. *Adv. Mater.* **2002**, *14*, 532.

(29) Zoldesi, C. I.; Imhof, A. *Adv. Mater.* **2005**, *17*, 924.

(30) Tsapis, N.; Bennett, D.; Jackson, B.; Weitz, D. A.; Edwards, D. A. *Proc. Natl. Acad. Sci.* **2002**, *99*, 12001.

(31) Loscertales, I. G.; Barrero, A.; Guerrero, I.; Cortijo, R.; Marquez, M.; Ganan-Calvo, A. M. *Science* **2002**, *295*, 1695.

(32) Larsen, G.; Velarde-Ortiz, R.; Minchow, K.; Barrero, A.; Loscertales, I. G. *J. Am. Chem. Soc.* **2003**, *125*, 1154.

(33) (a) Rana, R. K.; Murthy, V. S.; Yu, J.; Wong, M. S. *Adv. Mater.* **2005**, *17*, 1145. (b) Yu, J.; Murthy, V. S.; Rana, R. K.; Wong, M. S. *Chem. Commun.* **2006**, *10*, 1097.

(34) McKenna, B. J.; Birkedal, H.; Bartl, M. H.; Deming, T. J.; Stucky, G. D. *Angew. Chem., Int. Ed.* **2004**, *43*, 5652.

(35) Patwardhan, S. V.; Clarson, S. J. *Polym. Bull.* **2002**, *48*, 367.

(36) Brunner, E.; Lutz, K.; Sumper, M. *Phys. Chem. Chem. Phys.* **2004**, *6*, 854.

(37) Rodriguez, F.; Glawe, D. D.; Naik, R. R.; Hallinan, K. P.; Stone, M. O. *Biomacromolecules* **2004**, *5*, 261.

(38) Kröger, N.; Lorenz, S.; Brunner, E.; Sumper, M. *Science* **2002**, *298*, 584.

(39) Manning, G. S. *Acc. Chem. Res.* **1979**, *12*, 443.

(40) Bhuiyan, L. B.; Vlachy, V.; Outhwaite, C. *Int. Rev. Phys. Chem.* **2002**, *21*, 1.

(41) Olvera de la Cruz, M.; Belloni, L.; Delsanti, M.; Dalbiez, J. P.; Spalla, O.; Drifford, M. J. *J. Chem. Phys.* **1995**, *103*, 5781.

(42) Spohr, E.; Hribar, B.; Vlachy, V. *J. Phys. Chem. B* **2002**, *106*, 2343.

(43) Schmitz, K. S. *Macroions in Solution and Colloidal Suspension*; VCH: New York, 1993.

(44) Xia, J. L.; Dubin, P. L.; Havel, H. A. *Macromolecules* **1993**, *26*, 6335.

(45) Solis, F. J.; Olvera de la Cruz, O. *J. Chem. Phys.* **2000**, *112*, 2030.

(46) De Robertis, A.; De Stefano, C.; Giuffre, O.; Sammartano, S. *J. Chem. Soc., Faraday Trans.* **1996**, *92*, 4219.

(47) De Stefano, C.; Giuffre, O.; Sammartano, S. *J. Chem. Soc., Faraday Trans.* **1998**, *94*, 2395.

(48) De Robertis, A.; De Stefano, C.; Giuffre, O.; Sammartano, S. *J. Chem. Eng. Data* **2001**, *46*, 1365.

(49) Nordmeier, E. *Macromol. Chem. Phys.* **1995**, *196*, 1321.

(50) Porasso, R. D.; Benegas, J. C.; van den Hoop, M.; Paoletti, S. *Phys. Chem. Chem. Phys.* **2001**, *3*, 1057.

(51) Lefaux, C. J.; Zimberlin, J. A.; Dobrynin, A. V.; Mather, P. T. *J. Polym. Sci., Part B: Polym. Phys.* **2004**, *42*, 3654.

(52) Hiemenz, P. C.; Rajagopalan, R. *Principles of Colloid and Surface Chemistry*, 3rd ed.; Marcel Dekker, Inc.: New York, 1997.

(53) Hunter, R. J. *Foundations of Colloid Science*, 2nd ed.; Oxford University Press: New York, 2001.

(54) Evans, D. F.; Wennerstrom, H. *The Colloidal Domain: Where Physics, Chemistry, Biology, and Technology Meet*, 2nd ed.; Wiley-VCH: New York, 1999.

(55) Crist, B.; Nesarikar, A. R. *Macromolecules* **1995**, *28*, 890.

(56) The high PAH concentration ensured a dense packing of aggregates on the glass slide.

(57) Sjoblom, J. *Encyclopedic Handbook of Emulsion Technology*; Marcel Dekker: New York, 2001.

(58) Bibette, J. *Emulsion Science: Basic Principles: Overview*; Springer: New York, 2002.

(59) Kabalnov, A. S.; Pertzov, A. V.; Shchukin, E. D. *J. Colloid Interface Sci.* **1987**, *118*, 590.